JOURNAL OF SPACECRAFT AND ROCKETS
Vol. 45, No. 4, July–August 2008

Low-Gravity Slosh Analysis for Cylindrical Tanks with Hemiellipsoidal Top and Bottom

M. Utsumi*
IHI Corporation, Yokohama 235-8501, Japan

DOI: 10.2514/1.35057

Low-gravity sloshing in a circular cylindrical tank with hemiellipsoidal top and bottom is investigated. It is shown that the mechanical model of the sloshing steeply varies at a certain liquid-filling level due to a steep change in the magnitude of the inertial term of the modal equation. This variation in the mechanical model increases when the height of the hemiellipsoidal top of the tank decreases. These results are due to the fact that the contact angle between the liquid surface and the tank wall is small for the low-gravity propellant sloshing problem. This paper also develops a real-time computation algorithm that can be used to determine each parameter of the mechanical model during operation of a space vehicle according to the changing liquid-filling level and Bond number. A Fourier expansion method is repeatedly applied to allow for the steep variation in the aforementioned mechanical model and the dependence of the mechanical model on the Bond number as well as the liquid-filling level. The accuracy of this algorithm is confirmed by comparing the results obtained by the slosh analysis and the algorithm.

Nomenclature

a	=	radius of cylindrical part of tank, m
Bo	=	Bond number
b	=	height of hemiellipsoidal part of tank, m
C	=	contact line
c	=	length of cylindrical part of tank, m
$\mathbf{e}_x$, $\mathbf{e}_y$, $\mathbf{e}_z$	=	unit vectors in x, y, and z directions
F	=	disturbed liquid surface
$\ddot{f}(t)$	=	acceleration of tank in x direction, m/s^2
g	=	gravitational acceleration, m/s^2
l_0, l_1	=	z coordinates of fixed and slosh masses, respectively, m
M	=	meniscus (undisturbed liquid surface)
m_0, m_1	=	fixed and slosh masses, respectively, kg
$\mathbf{N}_F$	=	unit normal vector of F pointing into liquid domain
$\mathbf{N}_M$	=	unit normal vector of M pointing into liquid domain
$\mathbf{N}_W$	=	unit normal vector of W pointing outward from liquid domain
p_C	=	static liquid pressure at contact line, N/m^2
p_g	=	gas pressure, N/m^2
p_l	=	liquid pressure, N/m^2
$q(t)$	=	modal coordinate, m
R, θ, φ	=	spherical coordinates
$R_F(\theta, \varphi, t)$	=	R coordinate of disturbed liquid surface F, m
$R_M(\theta)$	=	R coordinate of meniscus M, m
$R_{M\theta}$, $R_{M\theta\theta}$	=	$dR_M/d\theta$, $d^2R_M/d\theta^2$, m
$R_W(\theta)$	=	R coordinate of tank wall W, m
$R_{W\theta}$	=	$dR_W/d\theta$, m
V	=	liquid domain
W	=	tank wall
W_1, W_2	=	liquid-solid and gas-solid interfaces, respectively
z_0	=	z coordinate of intersection of meniscus and z axis, m
z_C	=	z coordinate of contact line of meniscus with tank wall, m
ε	=	1 and −1 when the origin of the spherical coordinates is above or below the tank, respectively
ζ	=	liquid surface displacement, m
θ_C	=	contact angle between meniscus and tank wall
θ'_C	=	contact angle between disturbed liquid surface and tank wall
ρ_f	=	liquid density, kg/m^3
σ, σ_1, σ_2	=	surface energy per unit area associated with liquid-gas, liquid-solid, and gas-solid interfaces, respectively, N/m
ϕ	=	velocity potential describing the liquid motion relative to the tank, m^2/s
ω	=	eigenfrequency of sloshing, rad/s
ω_f	=	excitation frequency, rad/s

I. Introduction

LOW-GRAVITY propellant sloshing is a potential source of disturbance which may be critical to the stability of space vehicles, because a large force may be produced by the propellant oscillating at its fundamental eigenfrequency in a partially filled tank [1]. Therefore, it is necessary to examine the slosh dynamics under low-gravity conditions and to represent the slosh dynamics in terms of an equivalent mechanical model.

Studies on low-gravity sloshing have been conducted for cylindrical tanks [2–7] and for arbitrary axisymmetric tanks [8–12]. One limitation of conventional slosh analysis methods is that analytical expressions for the characteristic functions of the liquid motion cannot be developed for arbitrary axisymmetric tanks. Numerical methods were applied instead, and computation time and cost increased dramatically when the computational mesh was refined. To solve this problem, previous papers [13,14] developed a new analytical method for determining the characteristic functions for arbitrary axisymmetric tanks. This method uses spherical coordinates whose origin is at the apex of the cone that is tangent to the tank wall at the contact line of the meniscus with the tank wall, thereby expressing the characteristic functions of the sloshing in terms of the Gaussian hypergeometric function irrespective of the generatrix shape of the tank. The dimension of the eigenvalue problem required for obtaining a sufficiently converged solution is low. Therefore, fast and cost-efficient computation can be conducted.

Received 9 October 2007; revision received 19 February 2008; accepted for publication 23 March 2008.

*Senior Researcher, Machine Element Department, Technical Research Laboratory, 1 Shin-Nakaharacho, Isogo-ku, Kanagawa Prefecture; masahiko_utsumi@ihi.co.jp.

In previous papers [13,14], a spherical tank was used as an illustrative example. It was confirmed that the present theoretical predictions for the eigenfrequency are in good agreement with the previous theoretical [9] and experimental [11,15] results. One purpose of the present paper is to investigate low-gravity sloshing in a circular cylindrical tank with hemiellipsoidal top and bottom subjected to lateral excitation, and to develop an equivalent mechanical model for the sloshing. Studies on this low-gravity sloshing problem are relatively scarce, although this type of tank is widely used. It is shown that parameters of the equivalent mechanical model steeply vary at the liquid-filling level at which the liquid surface contacts with the tank wall at the joint between the cylindrical part and the hemiellipsoidal top of the tank. The physical reason for this steep variation is examined.

Another practically important purpose of this paper is to develop a real-time computation algorithm for the parameters of the mechanical model. To determine the parameters during operation of a space vehicle, according to the changing liquid-filling level and Bond number, an algorithm that can be implemented by a small-scale online computer is required. Representation of the sloshing characteristics in terms of such an algorithm facilitates the design of controllers, taking into account the slosh dynamics. In the low-gravity sloshing problem, the parameters of the mechanical model depend not only on the liquid-filling level but also on the Bond number, and furthermore, the parameters steeply change with the variation in the liquid-filling level as mentioned earlier. For these reasons, the algorithm cannot be expressed in terms of commonly used polynomial functions. To solve this problem, a Fourier expansion method is applied in this paper.

II. Method of Solution

A. Computational Model

The geometry is defined as in Fig. 1. The tank is subjected to the lateral acceleration $\ddot{f}(t)$ in the x direction. Note that the static liquid surface M (meniscus) is curved strongly due to the surface tension effect. The meniscus M is a plane surface under normal gravity. Equations of the upper and lower hemiellipsoidal parts are given by

$$(r/a)^2 + [(z-b-c)/b]^2 = 1 \qquad (b+c \le z \le 2b+c) \tag{1}$$

$$(r/a)^2 + [(z-b)/b]^2 = 1 \qquad (0 \le z \le b) \tag{2}$$

The analysis is performed under the following assumptions:

1) The liquid motion is inviscid, incompressible, and irrotational.

2) The tank is rigid.

3) The oscillatory displacement of the liquid surface ζ from its equilibrium position M is small enough to be represented within the framework of the linear theory.

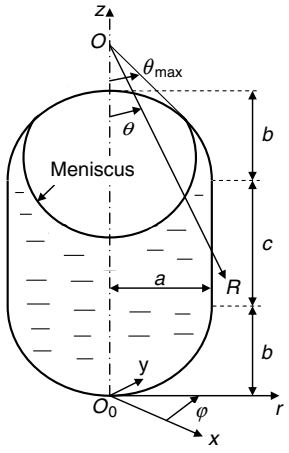

Fig. 1 Sloshing model and coordinate systems.

B. Spherical Coordinates

As shown in Fig. 1, we introduce spherical coordinates R, θ, and φ. The origin O is chosen as the apex of the cone whose side wall is tangent to the tank wall at the contact line of the meniscus. The liquid surface displacement ζ is considered in the R direction. In terms of the spherical coordinates, the undisturbed liquid surface M, disturbed liquid surface F, and the tank wall W are expressed as

$$M\colon\ R = R_M(\theta) \tag{3}$$

$$F\colon\ R = R_F(\theta,\varphi,t) = R_M(\theta) + \zeta(\theta,\varphi,t) \tag{4}$$

$$W\colon\ R = R_W(\theta) \tag{5}$$

When the tank wall is parallel to the z axis at the contact line of the meniscus, the spherical coordinates cannot be applied. To avoid this problem, the cylindrical part of the tank is considered an ellipsoidal surface given by

$$r^2/p_e^2 + (z-b-0.5c)^2/q_e^2 = 1 \quad \text{for} \quad b(1-\delta_1) \le z \le b+c+b\delta_1 \tag{6}$$

where δ_1 is a very small positive value, and p_e and q_e are determined such that r and $\mathrm{d}r/\mathrm{d}z$ at $z = b+c+b\delta_1$ calculated from Eq. (6) are equal to those determined from Eq. (1). Using these values of p_e and q_e, we can satisfy the condition that r and $\mathrm{d}r/\mathrm{d}z$ at $z = b(1-\delta_1)$ calculated from Eq. (6) coincide with those determined from Eq. (2). Through this slight modification of the tank geometry, the spherical coordinate expressions given by Eqs. (3–5) can be applied. When $\mathrm{d}r/\mathrm{d}z$ is positive at the contact line of the meniscus with the tank wall, the origin of the spherical coordinates is below the tank, in contrast to the case shown in Fig. 1.

C. Variational Principle

In this section, a variational principle is established, thereby deriving governing equations in a weighted-integral form. This form is required for the use of the Galerkin method. For the low-g sloshing problem, we must take into account the potential energy due to the gas pressure p_g and the surface energy associated with the liquid-gas, liquid-solid, and gas-solid interfaces. When the gas pressure and the surface energy are neglected, the Lagrangian per unit volume equals the liquid pressure p_l [16]. Therefore, the required variational principle can be expressed as

$$\delta \int_{t_1}^{t_2} \left[\iiint_V (p_l - p_g)\,\mathrm{d}V - \iint_F \sigma\,\mathrm{d}F - \iint_{W_1} \sigma_1\,\mathrm{d}W_1 - \iint_{W_2} \sigma_2\,\mathrm{d}W_2 \right] \mathrm{d}t = 0 \tag{7}$$

The liquid pressure p_l can be expressed in terms of the velocity potential ϕ describing the liquid motion relative to the tank:

$$p_l = p_C - \rho_f \left\{ \partial\phi/\partial t + g\varepsilon[R_M(\theta_{\max})\cos\theta_{\max} - R\cos\theta] + R\sin\theta\cos\varphi\,\ddot{f}(t) + \frac{1}{2}(\nabla\phi)^2 + \dot{G}(t) \right\} \tag{8}$$

where $\dot{G}(t)$ is an arbitrary time function.

Substituting Eq. (8) into Eq. (7) and considering the variation with respect to ϕ, ζ, and G leads to

$$\int_{t_1}^{t_2}\Bigg\{\rho_f\iiint_V\nabla^2\phi\delta\phi\,\mathrm{d}V-\rho_f\iint_W\nabla\phi\cdot\mathbf{N}_W\delta\phi\,\mathrm{d}W$$
$$-\rho_f\iint_F[(\partial\zeta/\partial t)\cos(\mathbf{N}_F,R)-\nabla\phi\cdot\mathbf{N}_F]\delta\phi\,\mathrm{d}F$$
$$+\iint_F(p_g-p_l-\sigma\mathrm{div}\mathbf{N}_F)\delta\zeta\cos(\mathbf{N}_F,R)\,\mathrm{d}F$$
$$+\varepsilon\int_C(\sigma\cos\theta'_C+\sigma_1-\sigma_2)\delta\zeta\,\mathrm{d}C$$
$$-\rho_f\delta G\iint_F(\partial\zeta/\partial t)\cos(\mathbf{N}_F,R)\,\mathrm{d}F\Bigg\}\mathrm{d}t=0 \tag{9}$$

Detailed explanations for the derivation of Eq. (9) are presented in the Appendix. The coefficients of the variations in Eq. (9) are made equal to zero to obtain a system of governing equations, which represent the condition of continuity in the liquid domain V, the kinematic boundary condition on the tank wall W, the kinematic and dynamic boundary conditions on the liquid surface F, the contact angle condition along the contact line C, and the liquid volume constant condition. The volume constant condition can be derived from the other kinematic conditions.

We express $\mathbf{N}_F$, $\mathbf{N}_W$, $\mathrm{d}F$, $\mathrm{d}W$, $\mathrm{d}C$, and $\cos\theta'_C$ in Eq. (9) in terms of the spherical coordinates introduced in Sec. II.B. We then employ the linear approximation for the boundary conditions on the disturbed liquid surface F, expressed by Eq. (4), and use the static equations that are used to determine the meniscus shape. We can thus transform Eq. (9) into

$$\rho_f\int_0^{2\pi}\int_0^{\theta_{\max}}\varepsilon\int_{R_M}^{R_W}\nabla^2\phi\delta\phi R^2\sin\theta\,\mathrm{d}R\,\mathrm{d}\theta\,\mathrm{d}\varphi$$
$$-\rho_f\int_0^{2\pi}\int_0^{\theta_{\max}}\varepsilon\left(\frac{\partial\phi}{\partial R}\bigg|_{R=R_W}-\frac{R_{W\theta}}{R_W^2}\frac{\partial\phi}{\partial\theta}\bigg|_{R=R_W}\right)$$
$$\times\delta\phi|_{R=R_W}R_W^2\sin\theta\,\mathrm{d}\theta\,\mathrm{d}\varphi$$
$$+\rho_f\int_0^{2\pi}\int_0^{\theta_{\max}}\varepsilon\left(\frac{\partial\phi}{\partial R}\bigg|_{R=R_M}-\frac{R_{M\theta}}{R_M^2}\frac{\partial\phi}{\partial\theta}\bigg|_{R=R_M}-\frac{\partial\zeta}{\partial t}\right)$$
$$\times\delta\phi|_{R=R_M}R_M^2\sin\theta\,\mathrm{d}\theta\,\mathrm{d}\varphi$$
$$+\int_0^{2\pi}\int_0^{\theta_{\max}}\left\{\varepsilon\rho_f\frac{\partial\phi}{\partial t}\bigg|_{R=R_M}+\varepsilon\rho_f R_M\sin\theta\cos\varphi\ddot{f}(t)\right.$$
$$-\rho_f g\zeta\cos\theta-\sigma\left[S_M^{(1)}(\theta)\zeta+S_M^{(2)}(\theta)\frac{\partial\zeta}{\partial\theta}+S_M^{(3)}(\theta)\frac{\partial^2\zeta}{\partial\theta^2}\right.$$
$$\left.\left.+S_M^{(4)}(\theta)\frac{\partial^2\zeta}{\partial\varphi^2}\right]\right\}\times\delta\zeta R_M^2\sin\theta\,\mathrm{d}\theta\,\mathrm{d}\varphi$$
$$-\int_0^{2\pi}\sigma\left[R_M(R_M^2+R_{M\theta}^2)^{-3/2}\left(R_M\frac{\partial\zeta}{\partial\theta}-R_{M\theta}\zeta\right)\right]_{\theta=\theta_{\max}}$$
$$\times\delta\zeta|_{\theta=\theta_{\max}}R_M(\theta_{\max})\sin\theta_{\max}\,\mathrm{d}\varphi=0 \tag{10}$$

where $S_M^{(i)}$ $(i=1$–$4)$ are functions expressed in terms of the meniscus shape $R_M(\theta)$.

D. Modal Equation

Because the Laplace equation is separable for the spherical coordinates, the vibration modes of ϕ and ζ can be analytically expressed as

$$\phi(R,\theta,\varphi)=i\omega\sum_{k=1}^{\infty}[a_k(R/l_a)^{\alpha_{1k}}+b_k(R/l_b)^{\alpha_{2k}}]\Theta_k(\theta)\cos\varphi e^{i\omega t} \tag{11}$$

$$\zeta(\theta,\varphi)=\sum_{k=1}^{\infty}c_k\Theta_k(\theta)\cos\varphi e^{i\omega t} \tag{12}$$

where a_k, b_k, and c_k are unknown real constants, l_a and l_b are normalization parameters, and α_{1k} and α_{2k} are characteristic exponents related to the separation variable λ by $\alpha(\alpha+1)=\lambda$:

$$\alpha_{1k}=(1/2)[-1-(1+4\lambda_k)^{1/2}]$$
$$\alpha_{2k}=(1/2)[-1+(1+4\lambda_k)^{1/2}] \tag{13}$$

Using $\alpha=\alpha_{1k}$ or $\alpha=\alpha_{2k}$, the characteristic function Θ_k can be expressed in term of the Gaussian hypergeometric series F:

$$\Theta_k(\theta)=\sin\theta F(1-\alpha,\alpha+2,2,(1-\cos\theta)/2) \tag{14}$$

The characteristic value λ_k is determined from the boundary condition

$$\mathrm{d}\,\Theta_k/\mathrm{d}\theta=0\quad\text{at }\theta=\theta_{\max} \tag{15}$$

Equation (15) is the kinematic condition at the contact line, because the θ direction is normal to the tank wall at the contact line.

For the spherical coordinates introduced in this study, $\theta_{\max}$ is smaller than $\pi/2$ (see Fig. 1), in contrast to the ordinary spherical coordinates defined in the range $0\le\theta\le\pi$. Hence, Θ_k is not the widely used associated Legendre polynomial but an infinite series [Eq. (14)] derived anew here. Because this series converges for $|(1-\cos\theta)/2|<1$, that is, $0\le\theta<\pi$ and $\theta_{\max}$ does not exceed $\pi/2$, the convergence is rapid. Thus, the application of the curvilinear coordinates for which the Laplace equation is separable leads to a computationally efficient semi-analytical method.

Substituting Eqs. (11) and (12) into Eq. (10), neglecting the excitation term, and applying the Galerkin method while considering variation for a_k, b_k, and c_k, leads to algebraic equations for a_k, b_k, and c_k. One important point is that these equations can be reduced to a computationally efficient standard eigenvalue problem for c_k alone by virtue of the factor $i\omega$ introduced in Eq. (11).

Substituting the fundamental mode solution of this eigenvalue problem into Eqs. (11) and (12) and replacing $e^{i\omega t}$, $i\omega e^{i\omega t}$ in these equations by the modal coordinate $q(t)$ and $\dot{q}(t)$ gives the expressions of ϕ and ζ for the forced vibration analysis. Substituting these expressions into Eq. (10) and considering the variation with respect to $q(t)$ leads to the modal equation of the form

$$M_0\ddot{q}+K_0q=\beta_0\ddot{f}(t) \tag{16}$$

that is

$$\ddot{q}+\omega^2q=\beta\ddot{f}(t) \tag{17}$$

where

$$\omega^2=K_0/M_0,\qquad\beta=\beta_0/M_0 \tag{18}$$

E. Equivalent Mechanical Model

The liquid force in the x direction can be calculated by

$$\hat{F}_x=\iint_{W_1}p_l(\mathbf{N}_W\cdot\mathbf{e}_x)\,\mathrm{d}W_1+\iint_{W_2}p_g(\mathbf{N}_W\cdot\mathbf{e}_x)\,\mathrm{d}W_2$$
$$+\int_C\sigma\frac{\mathbf{N}_F\times(\mathbf{N}_F\times\mathbf{N}_W)}{|\mathbf{N}_F\times(\mathbf{N}_F\times\mathbf{N}_W)|}\cdot\mathbf{e}_x\,\mathrm{d}C \tag{19}$$

The third term on the right-hand side represents the force due to the surface tension exerted along the moving contact line C. The integrand for this force can be derived from the fact that the surface tension force vector having the magnitude σ is perpendicular to the contact line C and is tangent to the oscillating liquid surface.

The dynamic component of the force, given by the first and second terms on the right-hand side of Eq. (19), can be expressed as Eq. (20) by using Eq. (8) and expressing the surface elements of the dynamic variations in W_1 and W_2 as $\mathrm{d}W_{1,\,\mathrm{dy}}=-\mathrm{d}W_{2,\,\mathrm{dy}}=-\varepsilon\zeta\,\mathrm{d}C_{\mathrm{st}}$.

$$\iint_{W_{1,\mathrm{st}}} p_{l,\mathrm{dy}}(\mathbf{N}_W \cdot \mathbf{e}_x)\,\mathrm{d}W_{1,\mathrm{st}} + \iint_{W_{1,\mathrm{dy}}} p_{l,\mathrm{st}}(\mathbf{N}_W \cdot \mathbf{e}_x)\,\mathrm{d}W_{1,\mathrm{dy}} + \iint_{W_{2,\mathrm{dy}}} p_g(\mathbf{N}_W \cdot \mathbf{e}_x)\,\mathrm{d}W_{2,\mathrm{dy}} = \iint_{W_{1,\mathrm{st}}} (-\rho_f)[\partial\phi/\partial t + x\ddot{f}(t)](\mathbf{N}_W \cdot \mathbf{e}_x)\,\mathrm{d}W_{1,\mathrm{st}} + \int_{C_{\mathrm{st}}} \varepsilon(p_g - p_C)\zeta(\mathbf{N}_W \cdot \mathbf{e}_x)\,\mathrm{d}C_{\mathrm{st}} \tag{20}$$

The dynamic component of the third term on the right-hand side of Eq. (19) can be expressed in terms of the liquid surface displacement ζ by using Eq. (4). Thus, the dynamic component of the force given by Eq. (19) can be expressed in terms of the modal coordinate $q(t)$ of the form

$$F_x = A_1\ddot{q}(t) + B_1\ddot{f}(t) + A_2 q(t) + A_3 q(t) \tag{21}$$

where A_1, B_1, A_2, and A_3 are constants arising from the integrations. The terms with A_1 and B_1 come from the first term on the right-hand side of Eq. (20), the term with A_2 comes from the second term on the right-hand side of Eq. (20), and the term with A_3 corresponds to the dynamic component of the third force in Eq. (19). The corresponding equation for the moment about the y axis can be obtained by altering $\mathbf{e}_x$ in Eqs. (19) and (20) to $\mathbf{e}_x z - \mathbf{e}_z x$. Therefore, the moment can be expressed of the same form:

$$M_y = C_1\ddot{q}(t) + D_1\ddot{f}(t) + C_2 q(t) + C_3 q(t) \tag{22}$$

The responses of the slosh force and moment to the sinusoidal excitation $\ddot{f}(t) = \sin\omega_f t$ can be calculated from Eqs. (17), (21), and (22) as

$$F_x = \frac{A_1\beta\omega_f^2 + B_1\left(\omega_f^2 - \omega^2\right) - (A_2 + A_3)\beta}{\omega_f^2 - \omega^2}\sin\omega_f t \tag{23}$$

$$M_y = \frac{C_1\beta\omega_f^2 + D_1\left(\omega_f^2 - \omega^2\right) - (C_2 + C_3)\beta}{\omega_f^2 - \omega^2}\sin\omega_f t \tag{24}$$

On the other hand, for the mechanical model as shown in Fig. 2, the responses of the force $F_{x,\mathrm{mech}}$ and the moment $M_{y,\mathrm{mech}}$ to the sinusoidal excitation can be calculated as

$$F_{x,\mathrm{mech}} = \frac{k_1 - m_0\left(\omega_f^2 - \omega_{\mathrm{mech}}^2\right)}{\omega_f^2 - \omega_{\mathrm{mech}}^2}\sin\omega_f t \tag{25}$$

$$M_{y,\mathrm{mech}} = \frac{k_1 l_1 - m_0 l_0\left(\omega_f^2 - \omega_{\mathrm{mech}}^2\right) + m_1 g}{\omega_f^2 - \omega_{\mathrm{mech}}^2}\sin\omega_f t \tag{26}$$

where $\omega_{\mathrm{mech}} = (k_1/m_1)^{1/2}$. From the condition that $F_{x,\mathrm{mech}} = F_x$ and $M_{y,\mathrm{mech}} = M_y$ hold for an arbitrary frequency ω_f of the excitation, the parameters of the mechanical model can be determined as

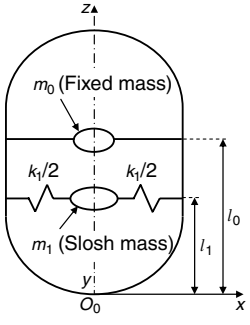

Fig. 2 Mechanical model.

$$m_0 = -A_1\beta - B_1 \tag{27a}$$

$$m_1 = A_1\beta - (A_2 + A_3)\beta/\omega^2 \tag{27b}$$

$$k_1 = m_1\omega^2 \tag{27c}$$

$$l_0 = -(C_1\beta + D_1)/m_0 \tag{27d}$$

$$l_1 = [-m_0 l_0\omega^2 - D_1\omega^2 - (C_2 + C_3)\beta - m_1 g]/k_1 \tag{27e}$$

F. Real-Time Computation Algorithm for Mechanical Model

Through the numerical calculation based on the foregoing slosh analysis method, we can examine the variations in the parameters of the mechanical model with the liquid-filling level and the Bond number. However, for practical applications, a real-time computation algorithm for these parameters is required to determine the mechanical model during space vehicle operations according to the changing liquid-filling level and Bond number.

Let P be a certain parameter of the mechanical model. The dependence of P on the liquid-filling level u for a fixed value of $v \equiv \log_{10} Bo$ can be expressed as a continuous function by interpolating the discrete values $P(u_i, v)$ $(i = 1 - i_{\max}, 0 < u_1 < \cdots < u_{i_{\max}} < 1)$ that are numerically determined from the present slosh analysis method. The range over which the function is defined is extended to the region $0 \le u \le 1$ using the following extrapolation:

$$P(u, v) = P(u_1, v) + \frac{P(u_2, v) - P(u_1, v)}{u_2 - u_1}(u - u_1) \qquad (0 < u < u_1) \tag{28}$$

$$P(u, v) = P(u_{i_{\max}}, v) + \frac{P(u_{i_{\max}}, v) - P(u_{i_{\max}-1}, v)}{u_{i_{\max}} - u_{i_{\max}-1}}(u - u_{i_{\max}}) \qquad (u_{i_{\max}} < u < 1) \tag{29}$$

Therefore, the function $P(u, v)$ can be expressed in terms of a Fourier series with respect to the liquid-filling level u:

$$P(u, v) = f_1(v)u + f_2(v) + \sum_{m=1}^{m_{\max}} f_{3m}(v)\sin m\pi u \tag{30}$$

where

$$f_1(v) = P(1, v) - P(0, v), \qquad f_2(v) = P(0, v)$$
$$f_{3m}(v) = 2\int_0^1 [P(u, v) - f_1(v)u - f_2(v)]\sin m\pi u\,\mathrm{d}u \tag{31}$$

Note that for achieving the accuracy near the boundaries $u = 0$ and $u = 1$, the following two features of Eq. (30) are helpful:

1) The linear function $f_1(v)u + f_2(v)$ with respect to u satisfying the boundary conditions is introduced.

2) The Fourier series term whose base functions $\sin m\pi u$ vanish at the boundaries is used to express the residual from the linear term.

We repeat the foregoing procedure for various values of v, and define the coefficients given by Eq. (31) as continuous functions for v, by interpolating the discrete points numerically determined from the slosh analysis. We then express these functions in terms of the Fourier series over the range $v_{\min} \le v \le v_{\max}$:

$$f_1(v) = a_1 v + a_2 + \sum_{n=1}^{n_{\max}} a_{3n}\sin\left[\frac{n\pi(v - v_{\min})}{v_{\max} - v_{\min}}\right] \tag{32}$$

$$f_2(v) = b_1 v + b_2 + \sum_{n=1}^{n_{\max}} b_{3n} \sin\left[\frac{n\pi(v - v_{\min})}{v_{\max} - v_{\min}}\right] \tag{33}$$

$$f_{3m}(v) = c_{1m} v + c_{2m} + \sum_{n=1}^{n_{\max}} c_{3mn} \sin\left[\frac{n\pi(v - v_{\min})}{v_{\max} - v_{\min}}\right] \tag{34}$$

where

$$\begin{Bmatrix} a_1 \\ b_1 \\ c_{1m} \end{Bmatrix} = \frac{1}{v_{\max} - v_{\min}} \begin{Bmatrix} f_1(v_{\max}) - f_1(v_{\min}) \\ f_2(v_{\max}) - f_2(v_{\min}) \\ f_{3m}(v_{\max}) - f_{3m}(v_{\min}) \end{Bmatrix} \tag{35}$$

$$\begin{Bmatrix} a_2 \\ b_2 \\ c_{2m} \end{Bmatrix} = \frac{1}{v_{\max} - v_{\min}} \begin{Bmatrix} v_{\max} f_1(v_{\min}) - v_{\min} f_1(v_{\max}) \\ v_{\max} f_2(v_{\min}) - v_{\min} f_2(v_{\max}) \\ v_{\max} f_{3m}(v_{\min}) - v_{\min} f_{3m}(v_{\max}) \end{Bmatrix} \tag{36}$$

$$\begin{Bmatrix} a_{3m} \\ b_{3m} \\ c_{3mn} \end{Bmatrix} = \frac{2}{v_{\max} - v_{\min}} \int_{v_{\min}}^{v_{\max}} \begin{Bmatrix} f_1(v) - a_1 v - a_2 \\ f_2(v) - b_1 v - b_2 \\ f_{3m}(v) - c_{1m} v - c_{2m} \end{Bmatrix} \sin\left[\frac{n\pi(v - v_{\min})}{v_{\max} - v_{\min}}\right] \tag{37}$$

Here, the linear terms $a_1 v + a_2$, $b_1 v + b_2$, and $c_{1m} v + c_{2m}$ satisfying the boundary conditions are introduced, and the residuals from the linear terms are expressed in terms of the Fourier series terms whose base functions vanish at the boundaries $v = v_{\min}$ and $v = v_{\max}$. Furthermore, we should note that this algorithm employs $v = \log_{10} Bo$ instead of Bo as a variable, because the changing rate of the parameters of the mechanical model with the reduction of Bo is larger for small Bond numbers than it is for large Bond numbers.

III. Numerical Results

The numerical calculation is conducted using dimensionless quantities normalized by the characteristic length b, mass $\rho_f b^3$, and frequency $(g/b)^{1/2}$. The Bond number defined by

$$Bo = \rho_f g b^2 / \sigma \tag{38}$$

is used as a dimensionless parameter relating the magnitude of gravity to surface tension. Numerical results are presented for a wide range of the Bond number for the following reasons:

1) The Bond number is low for spaceflight, however, relatively high Bond numbers may be realized for rockets, in which the liquid may be under large gravitational acceleration with the order of the gravity near the surface of the Earth.

2) Numerical results covering a wide range of the Bond number are helpful to illustrate the difference between the results for low and high Bond numbers.

Figure 3 shows geometries of the static liquid surface for the case in which $b/a = c/a = 1$ and $\theta_C = 5$ deg. It can be seen that the static liquid surface is curved strongly when the Bond number is decreased.

Figures 4–7 show the dimensionless angular eigenfrequency, slosh mass, and attachment positions of the slosh and fixed masses, respectively, for the case in which $b/a = c/a = 1$ and $\theta_C = 5$ deg. In each figure, the values obtained by the slosh analysis and the real-time computation algorithm are compared. The results for the values of the fixed mass are not presented, because the sum of the slosh and fixed masses numerically computed based on this theory equals the liquid mass, satisfying the mass conservation. For all the parameters of the mechanical model, excellent agreement can be confirmed between the values obtained by the slosh analysis and the real-time computation algorithm. Thus, this algorithm can be applied to accurate real-time computation of the mechanical model during

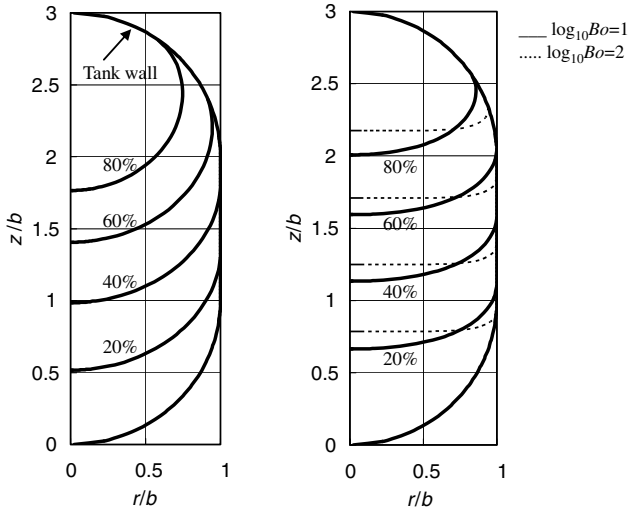

Fig. 3 Geometries of static liquid surface for liquid-filling levels of 20, 40, 60, and 80%: a) $\log_{10} Bo = 0$, b) $\log_{10} Bo = 1$ and $\log_{10} Bo = 2$.

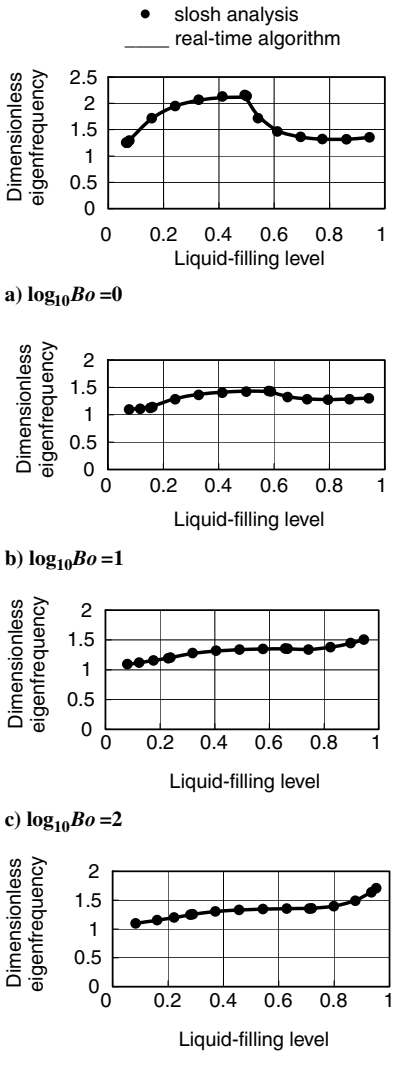

Fig. 4 Dimensionless angular eigenfrequency $(m_1/k_1)^{1/2}/(g/b)^{1/2}$ $(b/a = c/a = 1)$.

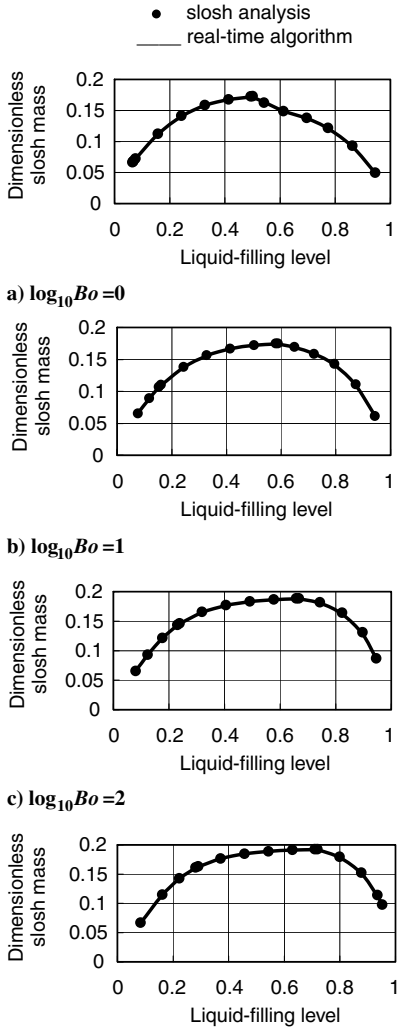

Fig. 5 Dimensionless slosh mass $m_1/\rho_f V_{\text{tank}}$ ($b/a = c/a = 1$).

operation of a spacecraft. Note that this algorithm remains accurate even when the parameters steeply change at a certain liquid-filling level for small Bond numbers, as is illustrated in Fig. 4a. This accuracy can be achieved by the Fourier series expansion technique.

To examine the physical reason for the steep change in the eigenfrequency shown by Fig. 4a, variations in several parameters with the liquid-filling level are shown in Figs. 8a–8c. It can be seen from Fig. 8a that, at the liquid-filling level yielding this steep change, z_C is equal to $2b = b + c$, that is, the contact line of the meniscus with the tank wall lies at the joint between the cylindrical and the upper hemiellipsoidal parts of the tank. This liquid-filling level is referred to as the critical liquid-filling level in this paper. Figure 8b shows that, at the critical liquid-filling level, the mass parameter M_0 of the modal Eq. (16) steeply increases as the liquid-filling level increases. However, the stiffness parameter K_0 does not exhibit steep change, as can be seen from Fig. 8b. Therefore, the steep reduction in the eigenfrequency $\omega = (K_0/M_0)^{1/2}$ shown in Fig. 4a originates in the steep increase of the mass parameter M_0 at the critical liquid-filling level. It can be seen from Figs. 8b and 8c that the variations in the mass parameter M_0 and the area of the meniscus with the liquid-filling level exhibit a similar tendency. This can be intuitively comprehended as follows. The mass parameter M_0 corresponds to the kinetic energy, which can be expressed in terms of a surface integral over the meniscus M using Green's theorem and the boundary condition $\partial\phi/\partial N_W = 0$ at the tank wall:

$$\frac{1}{2}\iiint_V (\nabla\phi)^2\,\mathrm{d}V = \frac{1}{2}\oiint_{M+W} \phi\frac{\partial\phi}{\partial N}\,\mathrm{d}S = \frac{1}{2}\iint_M \phi\frac{\partial\phi}{\partial N_M}\,\mathrm{d}M \quad (39)$$

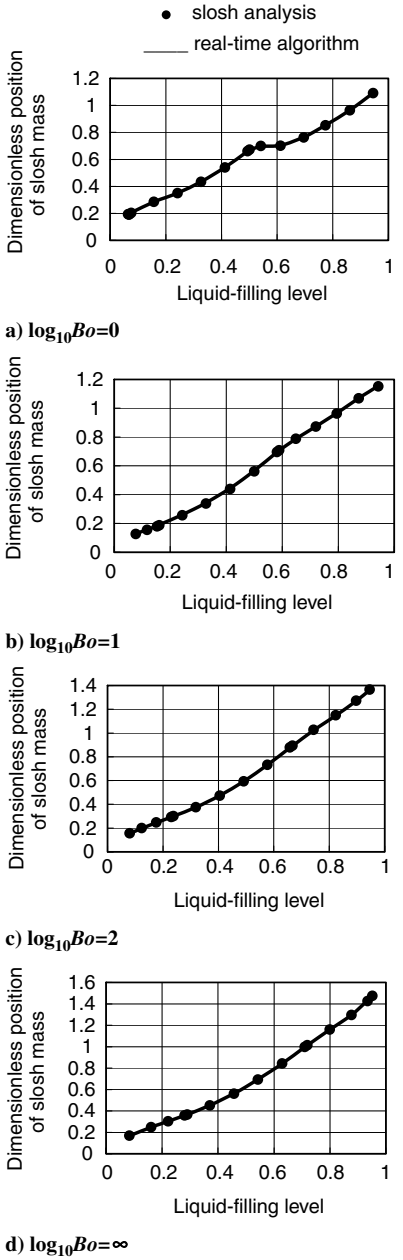

Fig. 6 Dimensionless position of slosh mass l_1/b ($b/a = c/a = 1$).

The value of this integral is greatly influenced by the area of the meniscus. Hence, the mass parameter and the area of the meniscus vary similarly with the liquid-filling level.

The steep change in the area of the meniscus results from the variations in z_C and z_0 shown in Fig. 8a. When the liquid volume V_{liquid} increases, $\partial z_0/\partial V_{\text{liquid}}$ decreases at the critical liquid-filling level, despite the discontinuous increase in $\partial z_C/\partial V_{\text{liquid}}$. The steep change in the area of the meniscus is due to the fact that the contact angle between the meniscus and the tank wall is small for the low-gravity propellant sloshing problem.

The magnitude of the steep change in the mechanical model is greatly influenced by the geometry of the upper hemiellipsoidal part of the tank. Figure 9 shows numerical results for a case in which b/a is decreased while keeping c/a the same. By comparing Figs. 8a and 8b with Figs. 4a and 5a, respectively, we see that the steep change in the mechanical model becomes more marked with the decrease in b/a. Here again, it can be confirmed that the proposed real-time computation algorithm remains accurate for the larger steep change in the mechanical model.

Comparison between Figs. 4a and 5a shows that the change at the critical liquid-filling level is larger for the eigenfrequency than for the

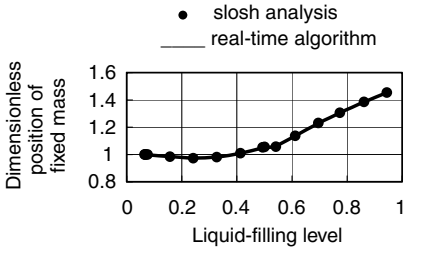

a) $\log_{10}Bo=0$

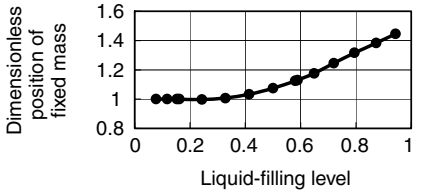

b) $\log_{10}Bo=1$

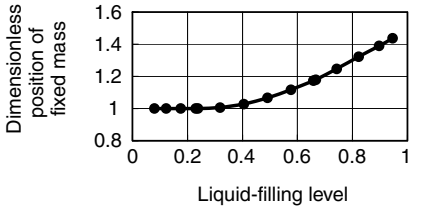

c) $\log_{10}Bo=2$

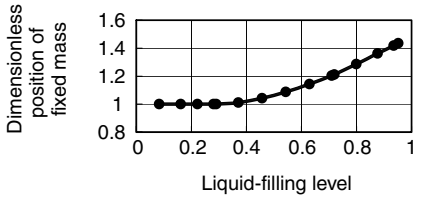

d) $\log_{10}Bo=\infty$

Fig. 7 Dimensionless position of fixed mass l_0/b ($b/a = c/a = 1$).

slosh mass. The reason for this can be explained by using Eq. (18) to express Eq. (27b) in terms of the mass parameter as

$$m_1 = A_1 \frac{\beta_0}{M_0} - \frac{M_0}{K_0}(A_2 + A_3)\frac{\beta_0}{M_0}$$

The change in the first term is not so large as the change in $1/M_0$, because the absolute values of A_1 and β_0 steeply increase at the critical liquid-filling level with the increase in the liquid-filling level. The second term is not influenced by the steep change in the mass parameter M_0. The change in β_0 is not so large as the change in M_0, and the constants A_2 and A_3, computed from the integrations along the contact line of the liquid surface with the tank wall, do not steeply change at the critical liquid-filling level.

Figure 5 shows that the range of the liquid-filling level, over which the value of the slosh mass is close to its maximum, is wider for large Bond numbers than for small Bond numbers. The reason for this can be explained as follows. The magnitude of the dynamic liquid pressure exerted along the generatrix $\varphi = 0$ of the tank wall is large near the contact point $z = z_C$. Hence, the magnitude of the slosh force is greatly influenced by the x component $\mathbf{N}_W \cdot \mathbf{e}_x$ of the unit normal vector $\mathbf{N}_W$ at the contact point. When the Bond number is decreased for a high fixed value of the liquid-filling level, the contact point goes up, reducing the value of $\mathbf{N}_W \cdot \mathbf{e}_x$ at the contact point. However, for a low fixed value of the liquid-filling level, the decrease in the Bond number does not result in the decrease in the x component $\mathbf{N}_W \cdot \mathbf{e}_x$ of

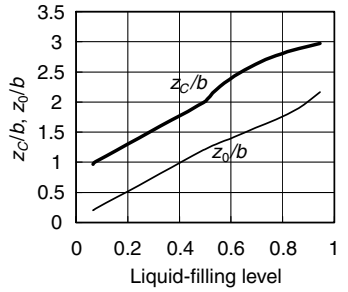

a) Normalized z coordinates z_c/b and z_0/b of contact line and lowest point of meniscus ($\log_{10}Bo=0$)

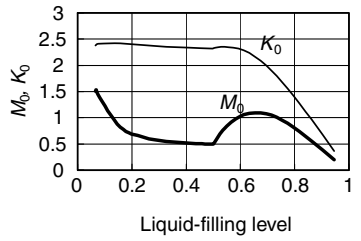

b) Mass and stiffness parameters M_0 and K_0 in modal Eq. (16) ($\log_{10}Bo=0$)

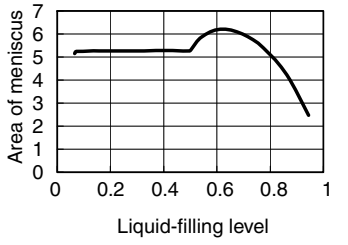

c) Area of meniscus ($\log_{10}Bo=0$)

Fig. 8 Dependence of various parameters on liquid-filling level ($b/a = c/a = 1$).

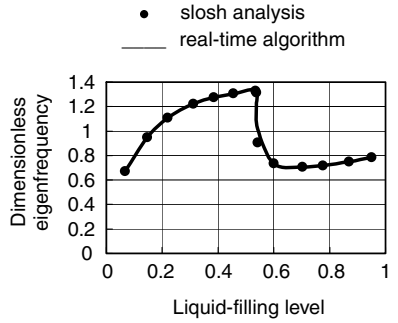

a) Dimensionless angular eigenfrequency $(m_1/k_1)^{1/2}/(g/b)^{1/2}$

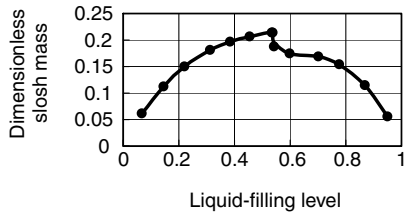

b) Dimensionless slosh mass $m_1/\rho_f V_{\text{tank}}$

Fig. 9 Results for a smaller value of b/a ($b/a = 0.625$; $c/a = 1$; $\log_{10}Bo = 0$).

the normal vector $\mathbf{N}_W$ at the contact point. Therefore, the slosh mass does not decrease with the reduction of the Bond number.

It can be seen from Fig. 6 that, when the Bond number is small, $\partial l_1/\partial V_{\text{liquid}}$ steeply decreases at the critical liquid-filling level $z_C = b + c$. This is because Eq. (27e) can be transformed into

$$\frac{l_1}{b} = \frac{1}{b}\frac{\omega^2 C_1 - (C_2 + C_3)}{\omega^2 A_1 - (A_2 + A_3)} - \frac{1}{\omega^2/(g/b)} \tag{40}$$

and the subtracted quantity $[\omega^2/(g/b)]^{-1}$ steeply increases at the critical liquid-filling level, as can be seen from Fig. 4a. In contrast to l_1, the attachment position l_0 of the fixed mass does not include the eigenfrequency ω, as can be seen from Eqs. (27a) and (27d). Therefore, the change in $\partial l_0/\partial V_{\text{liquid}}$ at the critical liquid-filling level $z_C = b + c$ is small, even when the Bond number is small, as is illustrated in Fig. 7a. Another significant observation that can be made from Fig. 7 is that l_0/b tends to one as the liquid-filling level decreases. This is because for the lower spherical part of the tank, the relation $(\mathbf{N}_W \cdot \mathbf{e}_x)z - (\mathbf{N}_W \cdot \mathbf{e}_z)x = b(\mathbf{N}_W \cdot \mathbf{e}_x)$ holds. Because of this relation, the constants in Eqs. (21) and (22) satisfy $C_1 = bA_1$ and $D_1 = bB_1$, and hence the position of the fixed mass, which can be expressed as $l_0 = (C_1\beta + D_1)/(A_1\beta + B_1)$ using Eqs. (27a) and (27d), is equal to b.

IV. Conclusions

A newly developed slosh analysis method has been applied to the development of an equivalent mechanical model for low-gravity sloshing in a circular cylindrical tank with hemiellipsoidal top and bottom. It was shown that

1) The mechanical model steeply changes at the liquid-filling level at which the liquid surface contacts with the tank wall, at the joint between the cylindrical part and the hemiellipsoidal top.

2) The steep change in the mechanical model increases when the height of the hemiellipsoidal top decreases.

This steep change is caused by steep variation of the mass parameter of the modal equation with the liquid-filling level. The variation in the mass parameter can be explained by the dependence of the area of the meniscus on the liquid-filling level.

Furthermore, this paper developed a real-time computation algorithm for the mechanical model by applying a Fourier expansion method repeatedly. Because this method allows for the steep change in the mechanical model and two independent variables, the Bond number and the liquid-filling level, an accurate algorithm can be developed. The development of the accurate real-time computation algorithm requires the slosh analysis be conducted for many values of the liquid-filling level and the Bond number. The proposed fast and cost-efficient slosh analysis method serves as a helpful tool for this requirement.

Appendix: Derivation of Eq. (9)

Equation (2) can be transformed into

$$\int_{t_1}^{t_2}\left[\iiint_V \delta p_l \,\mathrm{d}V + \iiint_V (p_l - p_g)\delta(\mathrm{d}V) - \iint_F \sigma\delta(\mathrm{d}F) - \iint_{W_1} \sigma_1\delta(\mathrm{d}W_1) - \iint_{W_2} \sigma_2\delta(\mathrm{d}W_2)\right]\mathrm{d}t = 0 \tag{A1}$$

The term with δp_l can be expressed as Eq. (A2) by using Eq. (8).

$$\int_{t_1}^{t_2}\iiint_V \delta p_l \,\mathrm{d}V\,\mathrm{d}t = \int_{t_1}^{t_2}\iiint_V (-\rho_f)\left[\frac{\partial(\delta\phi)}{\partial t} + \nabla\phi\cdot\nabla(\delta\phi) + \delta\dot{G}\right]\mathrm{d}V\,\mathrm{d}t \tag{A2}$$

The volume integration of each term in the bracket can be transformed as

$$\iiint_V \nabla\phi\cdot\nabla(\delta\phi)\,\mathrm{d}V = -\iint_F \nabla\phi\cdot\mathbf{N}_F\delta\phi\,\mathrm{d}F + \iint_W \nabla\phi\cdot\mathbf{N}_W\delta\phi\,\mathrm{d}W - \iiint_V \nabla^2\phi\delta\phi\,\mathrm{d}V \tag{A3}$$

$$\iiint_V \frac{\partial(\delta\phi)}{\partial t}\,\mathrm{d}V = \frac{\partial}{\partial t}\iiint_V \delta\phi\,\mathrm{d}V + \iint_F \delta\phi\frac{\partial\zeta}{\partial t}\cos(N_F, R)\,\mathrm{d}F \tag{A4}$$

$$\iiint_V \frac{\partial(\delta G)}{\partial t}\,\mathrm{d}V = \frac{\partial}{\partial t}\iiint_V \delta G\,\mathrm{d}V + \iint_F \delta G\frac{\partial\zeta}{\partial t}\cos(N_F, R)\,\mathrm{d}F \tag{A5}$$

Equation (A3) can be derived by using Green's theorem. Equations (A4) and (A5) are based on the fact that the time derivative of an integral over a time-varying domain (the first term on the right-hand side of each equation) is equal to the sum of an integral of the time derivative of the integrand over the instantaneous domain (the left-hand side of each equation) and an integral of the outward flux of the integrand over the moving boundary surface. Using the condition that $\delta\phi$ and δG vanish at $t = t_1$ and $t = t_2$, Eq. (A2) can be transformed into

$$\int_{t_1}^{t_2}\iiint_V \delta p_l \,\mathrm{d}V\,\mathrm{d}t = \int_{t_1}^{t_2}\left\{\rho_f\iiint_V \nabla^2\phi\delta\phi\,\mathrm{d}V - \rho_f\iint_W \nabla\phi\cdot\mathbf{N}_W\delta\phi\,\mathrm{d}W - \rho_f\iint_F [(\partial\zeta/\partial t)\cos(\mathbf{N}_F, R) - \nabla\phi\cdot\mathbf{N}_F]\delta\phi\,\mathrm{d}F - \rho_f\delta G\iint_F (\partial\zeta/\partial t)\cos(\mathbf{N}_F, R)\,\mathrm{d}F\right\}\mathrm{d}t \tag{A6}$$

The variation $\delta(\mathrm{d}V)$ in Eq. (A1) can be expressed as

$$\delta(\mathrm{d}V) = \mathrm{d}(\delta V) = -\delta\zeta\cos(N_F, R)\,\mathrm{d}F \tag{A7}$$

The term for the surface energy σ in Eq. (A1) can be calculated as

$$-\iint_F \sigma\delta(\mathrm{d}F) = -\iint_F \sigma\mathrm{div}\mathrm{N}_F\delta\zeta\cos(N_F, R)\,\mathrm{d}F + \varepsilon\int_C \sigma\delta\zeta\cos\theta'_C\,\mathrm{d}C \tag{A8}$$

where the first term on the right-hand side is the virtual work done by the virtual displacement normal to F based on

$$\delta(\mathrm{d}F) = \mathrm{div}\mathbf{N}_F\delta\zeta\cos(N_f, R)\,\mathrm{d}F \tag{A9}$$

which can be derived by using the integration form of $\mathrm{div}\mathbf{N}_F$:

$$\mathrm{div}\,\mathbf{N}_F = \lim_{D\to 0}\left(\oint\!\!\!\oint \mathbf{N}_F\cdot\mathbf{n}\,\mathrm{d}A/D\right) \tag{A10}$$

where D is an arbitrary volume including the point at which $\mathbf{N}_F$ is erected, A is the closed surface bounding D, and $\mathbf{n}$ is the outer normal unit vector of A. Let D be the domain which the surface element penetrates during the virtual displacement $\delta\zeta\cos(N_F, R)$ from $\mathrm{d}F$ to $\mathrm{d}F_1$ (see Fig. A1). Then $\mathbf{N}_F\cdot\mathbf{n}$ is equal to -1 on $\mathrm{d}F$, $\cos[\delta(\partial\zeta/\partial\theta)] \cong 1$ on $\mathrm{d}F_1$, and zero on the other portion of A. And so, Eq. (A10) gives

$$\mathrm{div}\,\mathbf{N}_F = \frac{\mathrm{d}F_1 - \mathrm{d}F}{\mathrm{d}F\delta\zeta\cos(N_F, R)} = \frac{\delta(\mathrm{d}F)}{\mathrm{d}F\delta\zeta\cos(N_F, R)} \tag{A11}$$

which coincides with Eq. (A9).

On the other hand, the work done by the virtual displacement in the tangential direction of each surface element cancels out mutually over the surface F due to the interaction between the adjacent surface elements, and is reduced to an integral along C given by the second term on the right-hand side of Eq. (A8).

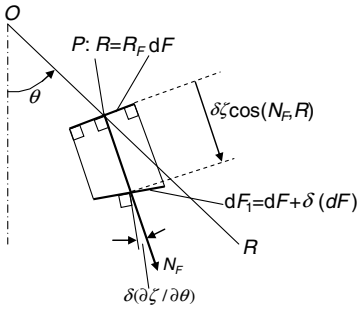

Fig. A1 Virtual displacement $\delta\zeta\cos(N_F, R)$ normal to liquid surface element $dF(\delta\zeta = \delta R_F)$.

The terms for the surface energies σ_1 and σ_2 in Eq. (A1) can be expressed as

$$-\iint_{W_1}\sigma_1\delta(\mathrm{d}W_1)-\iint_{W_2}\sigma_2\delta(\mathrm{d}W_2)=\varepsilon\int_C(\sigma_1-\sigma_2)\delta\zeta\,\mathrm{d}C \quad \text{(A12)}$$

by using $\delta(\mathrm{d}W_1)=-\delta(\mathrm{d}W_2)=-\varepsilon\delta\zeta\,\mathrm{d}C$. Substituting Eqs. (A6–A8) and (A12) into Eq. (A1) leads to Eq. (9).

References

[1] Abramson, H. N. (ed.), "Dynamic Behavior of Liquids in Moving Containers," NASA SP-106, 1966.

[2] Dodge, F. T., and Garza, L. R., "Experimental and Theoretical Studies of Liquid Sloshing at Simulated Low Gravity," *Journal of Applied Mechanics*, Vol. 34, Sept. 1967, pp. 555–562.

[3] Bauer, H. F., and Eidel, W., "Linear Liquid Oscillations in Cylindrical Container Under Zero-Gravity," *Applied Microgravity Technology*, Vol. 2, No. 4, 1990, pp. 212–220.

[4] Bauer, H. F., and Eidel, W., "Hydroelastic Vibrations in a Circular Cylindrical Container with a Flexible Bottom in Zero-Gravity," *Journal of Fluids and Structures*, Vol. 7, No. 7, 1993, pp. 783–802. doi:10.1006/jfls.1993.1046

[5] Yuanjun, H., Xingrui, M., Pingping, W., and Benli, W., "Low-Gravity Liquid Nonlinear Sloshing Analysis in a Tank Under Pitching Excitation," *Journal of Sound and Vibration*, Vol. 299, No. 1, 2007, pp. 164–177. doi:10.1016/j.jsv.2006.07.003

[6] Peterson, L. D., Crawley, E. F., and Hansman, R. J., "Nonlinear Fluid Slosh Coupled to the Dynamics of a Spacecraft," *AIAA Journal*, Vol. 27, No. 9, 1989, pp. 1230–1240.

[7] Satterlee, H. M., and Reynolds, W. C., "Dynamics of the Free Liquid Surface in Cylindrical Containers Under Strong Capillary and Weak Gravity Conditions," TR LG-2, Stanford Univ., Dept. of Mechanical Engineering, Stanford, CA, 1964.

[8] Chu, W. H., "Low-Gravity Fuel Sloshing in an Arbitrary Axisymmetric Rigid Tank," *Journal of Applied Mechanics*, Vol. 37, Sept. 1970, pp. 828–837.

[9] Concus, P., Crane, G. E., and Satterlee, H. M., "Small Amplitude Lateral Sloshing in Spheroidal Containers Under Low Gravitational Conditions," NASA CR-72500, 1969.

[10] Dodge, F. T., Green, S. T., and Cruse, M. W., "Analysis of Small-Amplitude Low Gravity Sloshing in Axisymmetric Tanks," *Microgravity Science and Technology*, Vol. 4, No. 4, 1991, pp. 228–234.

[11] Dodge, F. T., and Garza, L. R., "Simulated Low-Gravity Sloshing in Spherical, Ellipsoidal, and Cylindrical Tanks," *Journal of Spacecraft and Rockets*, Vol. 7, No. 2, 1970, pp. 204–206.

[12] Hung, R. J., Lee, C. C., and Leslie, F. W., "Similarity Rules in Gravity Jitter-Related Spacecraft Liquid Propellant Slosh Waves Excitation," *Journal of Fluids and Structures*, Vol. 6, No. 4, 1992, pp. 493–522. doi:10.1016/0889-9746(92)90028-2

[13] Utsumi, M., "Low-Gravity Propellant Slosh Analysis Using Spherical Coordinates," *Journal of Fluids and Structures*, Vol. 12, No. 1, 1998, pp. 57–83. doi:10.1006/jfls.1997.0125

[14] Utsumi, M., "Low-Gravity Sloshing in an Axisymmetrical Container Excited in the Axial Direction," *Journal of Applied Mechanics*, Vol. 67, June 2000, pp. 344–354. doi:10.1115/1.1307500

[15] Coney, T. A., and Salzman, J. A., "Lateral Sloshing in Oblate Spheroidal Tanks Under Reduced and Normal Gravity Conditions," NASA TN D-6250, 1971.

[16] Seliger, R. L., and Whitham, G. B., "Variational Principles in Continuum Mechanics," *Proceedings of the Royal Society of London, Series A: Mathematical and Physical Sciences*, Vol. 305, No. 1480, May 1968, pp. 1–25. doi:10.1098/rspa.1968.0103

L. Peterson
Associate Editor